Curvature-induced quantum spin-Hall effect on a Möbius strip

Kyriakos Flouris,[1,*] Miller Mendoza Jimenez,[1] and Hans J. Herrmann[2,3]
[1]*ETH Zürich, Computational Physics for Engineering Materials, Institute for Building Materials, Wolfgang-Pauli-Strasse 27, HIT, CH-8093 Zürich, Switzerland*
[2]*Departamento de Física, Universidade do Ceará, 60451-970 Fortaleza, Brazil*
[3]*CNRS, UMR 7636, PMMH, ESPCI, 10 rue Vauquelin, F-75231 Paris Cedex 5, France*

(Received 14 June 2021; revised 21 March 2022; accepted 13 May 2022; published 16 June 2022)

The quantum Hall effect has been predicted and discovered in various condensed-matter systems. A promising quantum material for such topological effects is graphene. We report the numerical observation of a curvature-induced spin-Hall effect in a monolayer graphene Möbius strip. The solution of the Dirac equation on the nontrivial and non-Euclidean manifold reveals that despite the absence of a Hall current, a spin-Hall current is a natural consequence for such a topology, as predicted from symmetry arguments.

DOI: 10.1103/PhysRevB.105.235122

I. INTRODUCTION

The discovery of the quantum Hall effect has triggered a surge of research in topological states of matter with a multitude of applications in quantum engineering and condensed-matter physics [1–3]. The topological invariants [4] of a system provide simplicity in the implementation, as well as protection from disorder [5]. Naturally, graphene has been extensively investigated in this context, carrying over its remarkable characteristics [6–8] into a topologically protected system. For example, the honeycomb bipartite lattice of graphene has been shown to exhibit the quantum Hall and the quantum spin-Hall effects in the presence of a magnetic field [9–11]. Nevertheless, a much more promising system would require breaking of the time invariance in a more intrinsic way without the need for an external field [12,13].

One such system is the simplest nontrivial fiber bundle, the famous Möbius strip [14,15]. Theoretical analysis has already hypothesized that a graphene Möbius strip can exhibit topological insulator properties owing to the zigzag edge states [16,17]. In this paper we show that a graphene Möbius strip inherently exhibits a quantum spin-Hall current. The strains induced in curved graphene are modeled via a non-Euclidean space description. The result is alluring because a pure, curved-space formulation of the lower energetic states of graphene would inevitably create a spin-Hall current and not a Hall current as theoretically predicted via symmetry arguments [18]. Furthermore, curvature has immense potential as a novel and straightforward control mechanism in quantum devices [19,20].

In this paper, we carry out a numerical study of the quantum spin-Hall effect on the curved-space solution of a graphene Möbius strip. We simulate Dirac particles and relate them to graphene through the low-energy approximation of the band structure. The effect of curvature on transport and the energy levels of confined Dirac particles on such a manifold are investigated. The nonrelativistic quantum mechanics on a Möbius strip has been studied [21], and nontrivial effects on the Möbius topology have also been proposed for molecular devices [22]. It has already been shown that in graphene, the quantum Hall effect can be realized with careful strain engineering in the zero-field case [23].

To this end numerical studies were carried out with a solver of the Dirac equation in curved space [24,25]. The method is based on the conceptual similarities between the Dirac and Boltzmann equations and is an extension of the quantum lattice Boltzmann method [26] to curved space. Through our simulations we observe a quantum spin-Hall current in the bulk of a Möbius graphene strip. Additionally, we compare the result to a simpler curved-space topology, namely, the torus, and we propose a simple valid current-conserving and time-reversal-symmetric boundary condition for the method. Furthermore, a specific illustration of the equivalence between the Berry and Ricci curvatures is presented analytically through a traveling wave packet around a Möbius strip.

II. THE DIRAC EQUATION IN CURVED SPACE

By minimally coupling the Dirac equation to curved space and a vector potential $A_i(x)$, the Dirac Hamiltonian takes the form

$$H_D = -i \int \Psi^\dagger \sigma^a e_a^i (\partial_i + \Gamma_i - iA_i) \Psi \sqrt{g} d^2x \qquad (1)$$

in natural units such that $\hbar = c = 1$, where $\hbar$ is Planck's constant and c is the speed of light (here, m is the particle mass, and $\mu = 0, 1, 2$ for two-dimensional space-time). Here, $\Psi = (\Psi^+, \Psi^-) = (\psi_1^+, \psi_2^-, \psi_1^-, \psi_2^+) \in \mathbb{C}^4$ denotes the spinor, and $\gamma^\mu = \gamma^\alpha e_\alpha^\mu$ are the generalized γ matrices, where $\gamma^\alpha \in \mathbb{C}^{4\times4}$ are the standard γ matrices (in Dirac representation). e_α^μ is the tetrad (first index: flat Minkowski, second index: curved space-time). Here, the tetrad is defined by $e_\alpha^\mu g_{\mu\nu} e_\beta^\nu = \eta_{\alpha\beta}$, where $g_{\mu\nu}$ denotes the metric tensor and $\eta_{\alpha\beta}$ is the Minkowski

*Corresponding author: kflouris@ethz.ch

metric. The tetrad basis is chosen such that the standard Dirac matrices can be utilized with no need to transform to a new coordinate basis. Γ_μ denotes the spin connection matrices given by $\Gamma_\mu = -\frac{i}{4}\omega_\mu^{\alpha\beta}\sigma_{\alpha\beta}$, where $\sigma_{\alpha\beta} = \frac{i}{2}[\gamma_\alpha, \gamma_\beta]$ and $\omega_\mu^{\alpha\beta} = \quad e_\nu^\alpha \nabla_\mu e^{\nu\beta}$. The Dirac equation in curved space describes quantum relativistic Dirac particles (e.g., electrons) moving on arbitrary manifold trajectories.

To model the single-layer carbon atom honeycomb lattice structure we start from the tight-binding Hamiltonian which is constructed assuming superposition of local wave functions for isolated atoms on a honeycomb lattice [27]. In the low-energy limit it has been shown that the tight-binding Hamiltonian converges to the Dirac Hamiltonian in the continuum limit. Therefore, for graphene the effective Hamiltonian is [28]

$$H_D^* = -iv_f \int \Psi^\dagger \sigma^a \left(v_a^{*i}\partial_i + \Gamma_a^* - iA_a^*\right)\Psi d^2x, \qquad (2)$$

where $v_a^{*i} = \delta_{ai} + u_{ai} - \beta\varepsilon_{ai}$ is the space-dependent Fermi velocity, $\Gamma_a^* = \frac{1}{2v_f}\partial_j v_a^{*j}$ is a complex gauge vector field which guarantees the Hermiticity of the Hamiltonian, and A_a^* is a strain-induced pseudovector potential given by $A_a^* = (A_x^*, A_y^*) = \frac{\beta}{2a}(\varepsilon_{xx} - \varepsilon_{yy}, -2\varepsilon_{xy})$, with β being the material-dependent electron Grüneisen parameter, a being the lattice spacing, and $\varepsilon_{ij} = u_{ij} + \frac{1}{2}\partial_i h \partial_j h$ being the general strain tensor with in-plane (u_{ij}) and out-of-plane (h) deformations. The term u_{ai} in v_a^{*i} can be interpreted as the deformation potential and is purely a geometric consequence due to lattice distortion; it does not depend on the material as long as it has the same topology. Comparing this to the standard Dirac Hamiltonian in curved space (1), we can match both Hamiltonians H_D and H_D^*. The numerical solutions are obtained with the quantum lattice Boltzmann method as described in Appendix A and Ref. [29].

III. METHOD AND RESULTS

A. Quantum spin-Hall effect on a Möbius strip

1. Geometry and boundary conditions

The system geometry is initialized to the Möbius strip by the discrete mapping (or chart)

$$h^\alpha(\theta, r) = \begin{pmatrix} [R + wr\cos(\eta\theta/2)]\cos(\theta) \\ [R + wr\cos(\eta\theta/2)]\sin(\theta) \\ wr\sin(\eta\theta/2) \end{pmatrix}, \qquad (3)$$

with $\theta \in \{-\pi, \pi\}$, $r \in \{-L_r/2, L_r/2\}$, half-width w, a midcircle of radius R, and number of turns η at height $z = 0$. L_r is the domain size across the radial direction; for simplicity we set $L_r/2 = 1$. In the simulations, we consider a square sheet with reverse periodic boundary conditions in one direction on a grid of size $l_\theta \times l_r = 512 \times 512$ or 100×100 nm^2, A_a; the external potential is set to zero.

The metric tensor can be computed from $h^\alpha(x, y)$, relating the positions of the atoms from the three-dimensional flat space (laboratory frame with the Minkowski metric) to the curved space by

$$g_{ij} = \frac{\partial h^\alpha(\theta, r)}{\partial x^i}\frac{\partial h^\beta(\theta, r)}{\partial x^j}\eta_{\alpha\beta}. \qquad (4)$$

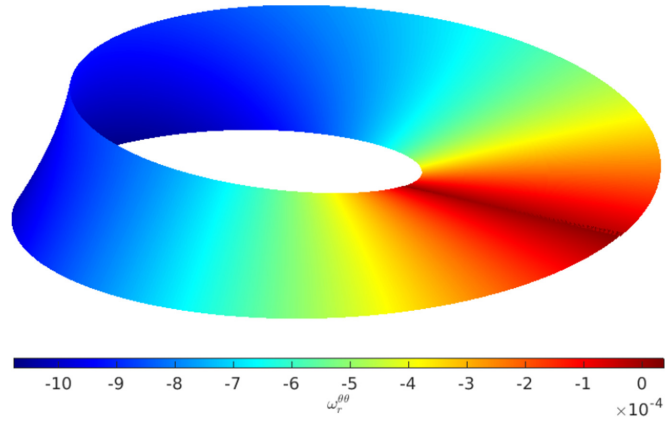

FIG. 1. The spin connection component on the Möbius strip for half-width $w = 0.1$ and a midcircle of radius $R = 1$.

With this parametrization the metric is cast in a diagonal form,

$$g_{ij} = \begin{pmatrix} G_{11}^2 & 0 \\ 0 & G_{22}^2 \end{pmatrix},$$

where $G_{11} = \sqrt{R + wr\cos(\eta\theta/2) + w^2r^2/4}$ and $G_{22} = w$. The reverse periodic boundary at $\theta = \pi$ is implemented as $\Psi(\theta = -\pi, r) = \Psi(\theta = \pi, -r)$. From Ref. [30] a valid current-conserving and time-reversal-symmetric boundary condition for the Dirac equation can be written as

$$\Psi = (\mathbf{v}\cdot\tau)\otimes(\mathbf{n}\cdot\sigma),\ \mathbf{n}\perp\mathbf{n}_B, \qquad (5)$$

where $\mathbf{n}_B$ is the unit vector in the r-θ plane normal to the boundary, $\mathbf{v}$ and $\mathbf{n}$ are three-dimensional unit vectors, and τ and σ are Pauli matrices. In the case of a massless particle inside a one-dimensional box, assuming perpendicular reflection, it is sufficient to set $\Psi_{1,2}(r = -1) = \Psi_{1,2}(r = 1) = 0$. This closed boundary condition ensures probability conservation for the decoupled Weyl equations such that $\rho(r = -1) = \rho(r = 1)$ and $J^\mu(r = -1) = J^\mu(r = 1) = 0$. Numerically, for the present simulational timescales, we observe a small (<1%), resolution-convergent error related to the finite-size effect of the wave function. The error convergence plot is shown in Appendix C.

The metric tensor, although diagonal, for the typical choice of $w \sim 1$ imposes some large gradients on the spin connection Γ^i which introduce numerical instabilities. From the form of the metric it can be shown that for $w \ll 1$, the metric variation is minimized, resulting in more stability; physically, this results in a long and thin strip. It should be noted that this choice of parametrization results in nonzero curvature across the whole domain, expressed by the Ricci scalar (see Appendix D). Additionally, θ is intentionally chosen such that the spin connection is continuous across the reverse periodic boundary (see Fig. 1). This is not the case for the most common convention $\theta \in \{0, 2\pi\}$. The spin connection (or the Christoffel symbols) is not a gauge-independent quantity, but the metric and Ricci tensors are. In fact, complete continuity of the spin connection is achieved only for $w \ll 1$; for $w \sim 1$ there is still some discrepancy as ω_i^{jk} is not symmetric in r.

2. Berry connection and symmetry arguments

Topological currents are traditionally described as being a consequence of the integral of the phase space connection, the Berry phase [31]. Analogous to the real-space curvature, the Berry connection is not gauge independent, but the Berry phase and the Berry curvature are. The similarities of the Ricci and Berry curvatures are further investigated here; we show that a Gaussian wave packet completing a circle around a Möbius strip will attain a phase π equivalent to a Berry phase. This is a consequence of the topology and represents a specific illustration of the relation between Berry and real-space curvatures [32].

To solve the Dirac equation, minimally coupled to curvature,

$$(i\gamma^{\mu}D_{\mu})\Psi = 0, \tag{6}$$

where D_{μ} is the covariant derivative as $D_{\mu}\Psi = \partial_{\mu}\Psi + \Gamma_{\mu}\Psi$, we assume that the wave packet has a negligible profile, $\delta\mathbf{r} \to 0$. The connection component of the covariant derivative can be absorbed into the wave function such that

$$\Psi \to \Psi \exp\left(i\int_{\mathbf{r}_c}^{\mathbf{r}_c+\delta\mathbf{r}} \Gamma_i d\mathbf{r}\right), \tag{7}$$

where $\mathbf{r}_c$ is the center of mass position and Γ_i is the spin connection matrix. For a Gaussian wave packet with spread σ and momentum $\mathbf{k}$

$$\Psi(\mathbf{r},\mathbf{k}) = \frac{1}{\sqrt{2\pi\sigma^2}}\begin{pmatrix}1\\0\\0\\-1\end{pmatrix} e^{i\int\Gamma_i d\mathbf{r}} e^{-\frac{|\mathbf{r}|^2}{4\sigma^2}+i\mathbf{k}\cdot\mathbf{r}}. \tag{8}$$

This wave function effectively minimally couples the standard Dirac equation to curved space through the spin connection. We define the Berry connection as

$$\mathcal{A}_n^i(\mathbf{R}) = i\langle\Psi(\mathbf{R})|\partial_{\mathbf{R}}|\Psi(\mathbf{R})\rangle \tag{9}$$

for some parameter space $\mathbf{R}$ and eigenfunction n. The Berry phase can be calculated from the complete loop integral of the connection,

$$\gamma = \oint_0^{2\pi} \mathcal{A}(\mathbf{R}) g^{ij}_{\mathbf{R}} d\mathbf{R}. \tag{10}$$

In a manner similar to the treatment of the Aharonov-Bohm effect from the Berry connection [31], we define the fast and slow coordinates as R and r, respectively, such that $\Psi(R) \to \Psi(r-R)$. For the Möbius strip, choosing the real space to be the parameter of integration and restricting the motion to one dimension $r \in 0, 2\pi$, the center of the band, the wave function takes the form

$$\Psi_r(R-r) = \frac{1}{\sqrt{2\pi\sigma^2}}\begin{pmatrix}1\\0\\0\\-1\end{pmatrix} e^{i\int\Gamma_r dr} e^{-\frac{|R-r|^2}{4\sigma^2}+ik(R-r)}. \tag{11}$$

From Eq. (9) the explicit form of the wave function implies that $\mathcal{A}^i = \mathrm{Tr}\Gamma_i$. The implication of this result is that the Berry connection and curvatures can be directly related to the real-space affine connection and Ricci curvature tensor under some conditions.

As a consequence, the phase change of a wave packet moving around a Möbius strip can be calculated from the Berry phase. Integrating naively around the band

$$\gamma = \oint_0^{2\pi} \mathrm{Tr}\langle\Psi_r|\partial_r\Psi_r\rangle g^{11} d\mathbf{r}, \tag{12}$$

where Tr denotes the trace of the resulting matrix and it takes into account the spinor nature of the Dirac wave function, yields a trivial result: $\gamma = 0$. The caveat is that, in this coordinate basis, for both half-width and half radius equal to unity, Γ_r simplifies to a diagonal matrix such that

$$\begin{pmatrix} \frac{1}{2}i\cos\left(\frac{r}{2}\right) & 0 & 0 & 0\\ 0 & -\frac{1}{2}i\cos\left(\frac{r}{2}\right) & 0 & 0\\ 0 & 0 & \frac{1}{2}i\cos\left(\frac{r}{2}\right) & 0\\ 0 & 0 & 0 & -\frac{1}{2}i\cos\left(\frac{r}{2}\right)\end{pmatrix}. \tag{13}$$

Γ_r is discontinuous when $\theta = 2\pi \to 0$. To make the function single valued we can perform a gauge transformation such that $\Psi \to \Psi' = \Psi e^{i\frac{r}{2}}$. This implies that $\gamma' = \gamma - \oint dr/2 = -\pi$. Therefore, the wave function picks up a phase of π as it moves around the band. This solutions clarifies the connection between the phase and real-space curvatures and emphasizes that a topological current is expected from geometrically nontrivial manifolds.

In the case of low-energy graphene, the calculated phase will be equal and opposite between the $k < 0$ and $k > 0$ states for a wave packet on the central line. To observe a nontrivial current for a graphene strip we need to depart from the center-line approximation, and the edges should be taken into consideration. Furthermore, since the phase will oscillate, the total Hall currents are expected to be zero, which is not the case for the spin-Hall currents, as explained also in Beugeling *et al.* [18]. The argument follows from the nonorientability of the Möbius strip, implying that any pseudovectorial field cannot be defined globally and smoothly on such a surface. The obvious consequence of this is the definition of a Chern number within such a topology. The introduction of spin-1/2 degrees of freedom creates a unique, orientable manifold that has an injective map of the original (base) space, i.e., an orientable double cover (ODC). Subjecting this ODC to a Haldane-like flux, by virtue of the geometry alone, two Haldane fluxes of opposite chirality are expected to develop for the particle-hole pair. This would be an intrinsic spin-orbit coupling inducing spin-Hall currents; that is, the two edge modes will counterpropagate.

3. Simulation

To study the topological properties and observe a Hall-type effect it is necessary to realize a forward-moving wave function that explores the complete domain. An electric field is both experimentally challenging and theoretically inconsistent across a periodic system such as a Möbius graphene strip. Additionally, a magnetic field is difficult to keep tangential to such a manifold and unnecessary, as shown later. Consequently, a wave function with nonzero k_θ is initialized in the

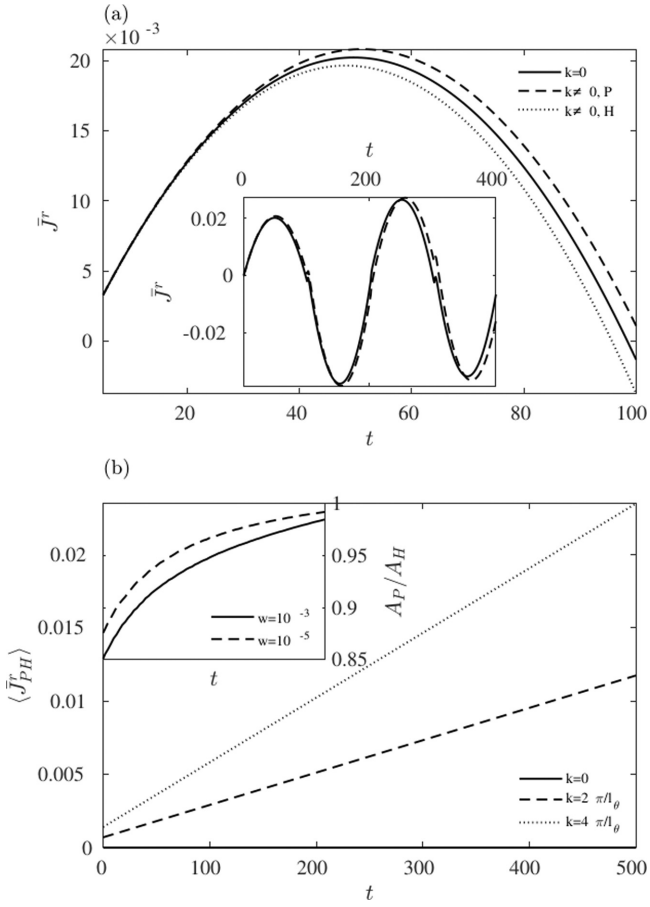

FIG. 2. (a) The time evolution of the radial space-integrated Dirac current $\bar{J}^r$ for the zero-momentum particle wave function and nonzero momentum particle and antiparticle wave functions. The inset shows the time evolution of $\bar{J}^r$ for a particle wave function for zero and nonzero momenta. (b) The time evolution of the average particle-hole space-integrated current for zero and two different nonzero k_θ. The inset shows the asymmetry ratio for two different half-widths w. One simulational time step t is equivalent to 1 ps.

domain for a particle and a hole, respectively,

$$\psi_P(\mathbf{k},\mathbf{r}) = \begin{pmatrix} i\sin(k_\theta\theta) \\ 0 \\ 0 \\ \frac{\hbar v_f \mathbf{k}}{E}\cos(k_\theta\theta) \end{pmatrix}, \quad \psi_H(\mathbf{k},\mathbf{r}) = \begin{pmatrix} 0 \\ \frac{\hbar v_f \mathbf{k}}{E}\cos(k_\theta\theta) \\ i\sin(k_\theta\theta) \\ 0 \end{pmatrix}, \tag{14}$$

where $\hbar = v_f = 1$, $E = |k|$, $\mathbf{r} = (\theta, r)$, and $\mathbf{k} = (k_\theta, k_r)$, $k_r = 0$.

In this section the subscript θ is dropped for brevity, $k_\theta \to k$. The time evolution of the radial space-integrated Dirac current

$$\bar{J}^r = \left(\int^{x,y} J^r(x,y)\sqrt{g}dxdy \right) \tag{15}$$

for ψ_P is shown in Fig. 2(a) for the zero-momentum and $k = 2\pi/l_\theta$ cases for both the particle and hole wave functions. The dashed and dotted lines lie on opposite sides relative to the $k_\theta = 0$ scenario, indicating a net anomalous velocity effect (in the r direction) as a consequence of θ velocity, i.e., a Hall current. The time evolution of $\bar{J}^r_P$ and $\bar{J}^r_{P,k=0}$ for longer times is plotted in the inset of Fig. 2(a). The oscillations are a result of the geometry and the closed boundary condition because they are also present for $\bar{J}^r_{P,k=0}$. There is no obvious nonzero average $\bar{J}^r_P$, or quantum Hall current.

The asymmetry ratio A_P/A_H is plotted in the inset of Fig. 2(b) for two different half-widths w, defined by

$$\frac{A_P}{A_H} = \frac{\bar{J}^r_P - \bar{J}^r_{P,k=0}}{\bar{J}^r_H - \bar{J}^r_{H,k=0}}, \tag{16}$$

where $\bar{J}^r_{P,H}$ denote the particle-hole currents for $k = 2\pi/l_\theta$ and $\bar{J}^r_{P,H,k=0}$ denote the particle-hole currents for $k = 0$. $\bar{J}^r_{P,k=0}$ and $\bar{J}^r_{H,k=0}$ are equal to each other. The dependence of the asymmetry ratio on w suggests that the difference between $\bar{J}^r_P$ and $\bar{J}^r_H$ is a consequence of the curvature of the manifold and implies, again, a net anomalous velocity effect.

In Fig. 2(b) the time evolution of the average particle-hole space-integrated current $\langle \bar{J}^r_{PH} \rangle = |\bar{J}^r_P - \bar{J}^r_H|$ is plotted for two different nonzero k. The result clearly shows a quantum spin-Hall current (or particle-antiparticle current), which is k_θ dependent. The effect is a transient result as there is no constant electric field in order to measure a stationary solution. Since a Möbius strip has only one boundary, it is easier to visualize the result when it is projected to a rectangle (simulational domain), where the current is flowing towards one direction.

The spin-Hall current is a consequence of the curvature and topology of the system. The gauge field breaking the symmetry of the system is the spin connection matrix Γ_i, similar to a twisting magnetic field. For graphene, these curvature effects are realized as forces due to the pseudopotential in a strained sheet [28]. The correspondence between a magnetic field and curvature is also evident in Sec. III A 2, as the Berry phase is directly related to the Aharanov-Bohm effect [33].

The space-integrated spin-Hall current is then a result of the topology, i.e., the twist. This can be understood theoretically as a space-integrated current would not be affected by the "sharpness" of the twist and any "flat" regions are irrelevant. Moreover, assuming geometrical disorder is not stronger than the cumulative effect of the twist, the bulk current will not be affected more than a perturbative correction.

Furthermore, it has been established that the quantum levels on the Möbius strip are quantized in k_θ for the Schrödinger equation (see Ref. [21]). Equivalently, this quantization is also expected for the Dirac equation; indeed, it is evident from the local density of states (LDOS) as calculated from the energy spectrum E_n of the system and its normalized eigenfunctions $\phi_n(x)$ according to the following relation:

$$\rho_{\mathrm{LDOS}}(x,E) = \frac{1}{\pi}\sum_n |\phi_n(x)|^2 \mathrm{Im}\frac{1}{E - E_n - i\delta\epsilon}. \tag{17}$$

$\delta\epsilon \approx 0.02$ eV is the approximate broadening of the energy spectrum peaks. The result is plotted in Fig. 3, where the discrete energy levels of the system are clearly visible. The current measured here is then quantized with respect to k_θ. Therefore, the response is identified as a quantum spin-Hall current, which can be used to define the Hall conductivity. Through symmetry arguments it was proposed that the

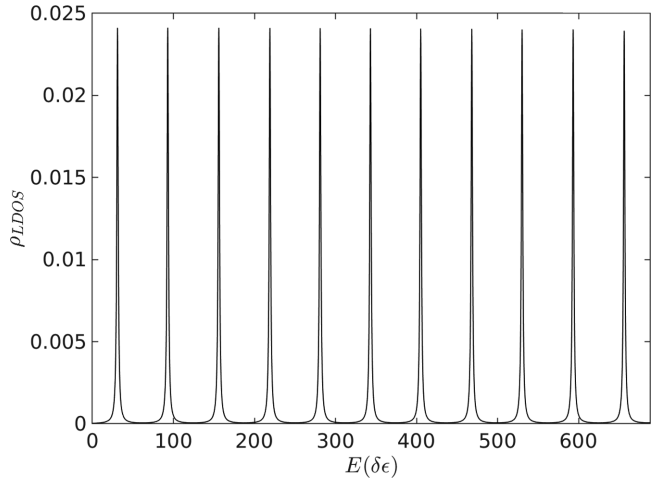

FIG. 3. Local density of states plotted against normalized energy at $\theta = r = 0$.

quantum Hall effect cannot exist on the Möbius strip but the quantum spin-Hall effect should be possible [18]. This result is also confirmed here through this direct simulation.

Experimental realizations of Möbius strips of single crystals of $NbSe_3$ have been reported [34], and recently, a supramolecular strategy for fabrication was proposed [35]. Graphene Möbius strips could be realized by similar methods or in combination with graphene shape-engineering tools such as optical forging [36]. It can be shown that a pulsed laser beam can forge a graphene sheet into controlled three-dimensional shapes in the nanoscale; therefore, two halves of a Möbius ribbon can be forged and further connected together [37]. Additionally, due to the topological nature of the current the result will be robust to any possible temperature fluctuation. $\bar{J}^r_{P,H}$ can be measured across r at a fixed k.

B. Curvature-induced Hall current on a torus

To investigate further the relevance of topology and curvature, a similar, but simpler, shape is also simulated. The system is initialized to the torus geometry by the discrete mapping,

$$h = \begin{pmatrix} [R + w\cos(\phi)]\cos(\theta) \\ [R + w\cos(\phi)]\sin(\theta) \\ w\sin(\theta) \end{pmatrix}, \tag{18}$$

with $\theta, \phi \in \{-\pi, \pi\}$, width w, a midcircle of radius R, where $R, w \in \mathbb{R}_{>0}$ and both boundaries are periodic. In this parametrization the metric is diagonal and ϕ dependent, $g_{ij} = \mathrm{diag}([R + w\cos(\phi)]^2, w^2)$. In Fig. 4 the time evolution of the azimuthal current $\bar{J}^\phi$ is plotted for particle (dotted line) and hole (dashed line) wave functions as before. The solid line represents a particle wave function with $k_\theta = 0$. Here, it is evident that an equivalent Hall current develops for both particles and holes in the presence of a θ velocity. The different geometry results in a simpler behavior, where a transverse current develops as a consequence of curvature. The net current and spin-Hall currents would be zero on a graphene torus. This result clarifies that the spin-Hall current observed in the previous section has a topological nature, developing from the introduction of the nontrivial topology, the Möbius strip.

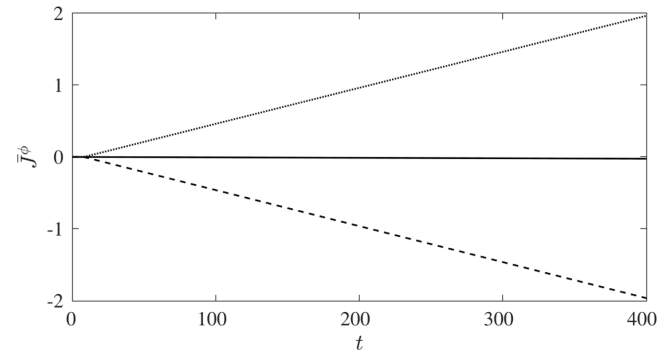

FIG. 4. The time evolution of the azimuthal current $\bar{J}^\phi$ for nonzero momentum particle (dotted line) and hole (dashed line) wave functions. The solid line represents a particle wave function with $k_\theta = 0$. One simulational time step t is equivalent to 1 ps.

IV. CONCLUSIONS AND OUTLOOK

We have presented a study of the topological and geometrical transport properties of a Möbius graphene strip. The challenges and resolutions in simulating such a system were outlined. The continuity of the spin connection was achieved by a gauge transformation and limiting the half-width of the strip.

In the absence of a magnetic field, we measured a quantum spin-Hall current on the graphene strip originating from topology and curvature, whereas a quantum Hall current was not observed. This result also represents an example of the correspondence between a magnetic field and a curved manifold. The torus geometry was simulated for comparison, where a Hall current is measured. Additionally, a concrete illustration of the equivalence between the Berry and Ricci curvatures was presented through a wave packet traveling around the Möbius strip.

Building on these results, higher-order and different types of topologies can be further investigated in the context of curvature. Without the need for a magnetic or electric field and by further understanding the properties of topological graphene sheets, simple and topologically robust quantum devices could be developed just by exploiting their geometry.

ACKNOWLEDGMENTS

The authors are grateful for the financial support from the Swiss National Science Foundation under Grant No. 200021 165497 and to Prof. S. Succi and I. Petrides for helpful conversations.

APPENDIX A: CURVED-SPACE QUANTUM LATTICE BOLTZMANN

The quantum lattice Boltzmann (QLB) method used for solving the Dirac equation as minimally coupled to curved space is an extension of the original method developed by Succi and Benzi [26]. The method exploits the conceptual similarities between the Dirac equation and the Boltzmann

equation on the lattice. We present here the QLB method for a three-dimensional manifold.

1. The Dirac equation

The Dirac equation can be naturally extended to curved space described by a metric tensor $g_{\mu\nu}$ with a covariant derivative D_μ as

$$(i\gamma^\mu D_\mu + m)\Psi = 0, \tag{A1}$$

where γ^μ denote the Dirac matrices.

The classical Boltzmann equation for a particle density distribution function $f(x_a, v_a, t)$ is given by

$$\partial_t f + v^i \partial_{x^i} f = \mathcal{C}[f] - F^a \partial_{v^a} f; \tag{A2}$$

the left-hand side describes the advection of the distribution function, velocity v^a, whereas the right-hand side describes the collisions between particles and the effect of external forces F^a. Furthermore, the Dirac equation in curved space (A1) can be cast into a kinetic theory form,

$$\partial_t \Psi + \sigma^a \partial_a \Psi = \mathcal{C}\Psi + \mathcal{F}\psi. \tag{A3}$$

Therefore, similar to the Boltzmann equation, the left-hand side represents the "free-streaming" step along matrix-valued "velocities" σ^i, while the right-hand side contains a "collision" and a "forcing" term.

The collision term in Eq. (A3) is represented by

$$\mathcal{C} = -\left(im\gamma^0 + \sigma^a e_a^i \Gamma_i\right), \tag{A4}$$

where m is the fermion mass. The forcing term is given by

$$\mathcal{F} = -\sigma^a \left(e_a^i - \delta_a^i\right)\partial_i, \tag{A5}$$

where the symbols have their usual meaning. The partial derivative of the Dirac equation is distributed between the streaming part and the forcing term, resulting in a lattice-compatible classical streaming operator of the form $\partial_t + v^a \partial_a$, where $v^a \in \mathbb{Z}$. The forcing term is a consequence of the generalized Dirac matrices $\gamma^i = e_a^i \gamma^a$ and captures the bulk of the curvature effects. The partial derivative in Eq. (A5) is approximated by a local finite-difference scheme.

2. Diagonal streaming operator

In order to obtain a diagonal streaming operator, the complex σ matrices have to be diagonalized first, which yields a diagonal velocity matrix with eigenvalues $v^a = \pm 1$. The diagonalization is achieved by suitable "rotation matrices":

$$X_a^\dagger \sigma^a X_a = \begin{pmatrix} 1 & 0 & 0 & 0 \\ 0 & 1 & 0 & 0 \\ 0 & 0 & -1 & 0 \\ 0 & 0 & 0 & -1 \end{pmatrix} = \gamma^0, \qquad a = 0, 1, 2,$$

where the unitary transformation matrices X_1, X_2, and X_3 are given by

$$X_1 = \tfrac{1}{\sqrt{2}} \begin{pmatrix} 1 & 0 & -1 & 0 \\ 0 & 1 & 0 & -1 \\ 0 & 1 & 0 & 1 \\ 1 & 0 & 1 & 0 \end{pmatrix}, \quad X_2 = \tfrac{1}{\sqrt{2}} \begin{pmatrix} 0 & i & 0 & 1 \\ -i & 0 & i & 0 \\ -1 & 0 & -1 & 0 \\ 0 & -1 & 0 & -i \end{pmatrix},$$

$$X_3 = \tfrac{1}{\sqrt{2}} \begin{pmatrix} 1 & 0 & 0 & -1 \\ 0 & 1 & 1 & 0 \\ 1 & 0 & 0 & -1 \\ 0 & 1 & 1 & 0 \end{pmatrix}.$$

The streaming and collision operations are performed in successive steps using operator splitting since the simultaneous diagonalization of the three σ matrices is not possible:

$$\Psi\left(t + \frac{\Delta t}{D}\right) = \exp\left[-\Delta t \sigma^1 \partial_1 + \frac{\Delta t}{D}(\mathcal{C} + \mathcal{F})\right]\Psi(t),$$

$$\Psi\left(t + \frac{2\Delta t}{D}\right) = \exp\left[-\Delta t \sigma^2 \partial_2 + \frac{\Delta t}{D}(\mathcal{C} + \mathcal{F})\right]\Psi\left(t + \frac{\Delta t}{D}\right),$$

$$\Psi(t + \Delta t) = \exp\left[-\Delta t \sigma^3 \partial_3 + \frac{\Delta t}{D}(\mathcal{C} + \mathcal{F})\right]\Psi\left(t + \frac{2\Delta t}{D}\right),$$

where $D = 3$ denotes the spatial dimensions. Each streaming step can be diagonalized by left multiplying with $X_a^\dagger$,

$$X_a^\dagger \Psi\left(t + \frac{\Delta t}{D}\right) = \exp[-\Delta t \sigma^a \partial_a + \Delta t(\tilde{\mathcal{C}}_a + \tilde{\mathcal{F}}_a)]\tilde{\Psi}_a(t), \tag{A6}$$

with the definitions

$$\tilde{\Psi}_a := X_a^\dagger \Psi, \ \tilde{\mathcal{F}}_a := \tfrac{1}{2} X_a^\dagger \mathcal{F} X_a, \ \tilde{\mathcal{C}}_a := \tfrac{1}{2} X_a^\dagger \mathcal{C} X_a$$

for $a = 1, 2, 3$ (no Einstein summation is used here). The exponential is approximated as

$$\exp[-\Delta t \sigma^a \partial_a + \Delta t(\tilde{\mathcal{C}} + \tilde{\mathcal{F}})] \approx \left[\mathbb{I} - \Delta t \sigma^a \partial_a + \Delta t(\tilde{\mathcal{C}}_a + \Delta t \tilde{\mathcal{F}}_a) + \left(\mathbb{I} - \frac{\Delta t}{2}\tilde{\mathcal{C}}_a\right)^{-1}\left(\mathbb{I} + \frac{\Delta t}{2}\tilde{\mathcal{C}}_a\right)\right].$$

The expansion of the collision operator $e^{\Delta t\tilde{\mathcal{C}}_a}$ is unitary and thus conserves exactly the probability of the wave function. The streaming $e^{-\Delta t\gamma^0\partial_a}$ and forcing $e^{\Delta t\tilde{\mathcal{F}}_a}$ operators are not expanded because this is prohibited by the derivative. A simple second-order expansion is performed, limiting the probability norm to Δt^2 accuracy. The operator splitting implies an error of order $O(\Delta t^2)$, as $e^{\Delta tX}\cdot e^{\Delta tY} = e^{\Delta t(X+Y)+1/2\Delta t^2[X,Y]} = e^{\Delta t(X+Y)} + O(\Delta t^2)$.

The manifold is described by a chart h defined in linear space, discretized on a regular rectangular lattice. The curved space quantum lattice Boltzmann method evolves the four-spinor $\Psi = (\Psi^+, \Psi^-) = (\Psi_1^+, \Psi_2^-, \Psi_1^-, \Psi_2^+)$ from t to $t+\delta t$. Once the operators are split, the following algorithm is performed in sequence for each lattice direction n_a, where $n_1 = (1,0)$, $n_2 = (0,1)$, and $a = 1, 2$.

(1) **Rotation:** The spinor is rotated by X_a,

$$\tilde{\Psi}_a(x,t) = X_a^\dagger \Psi(x,t). \tag{A7}$$

(2) **Collisions and curvature:** The collision and force operators are applied to the rotated spinor,

$$\tilde{\Psi}_a^*(x,t) = \left[\Delta t\tilde{\mathcal{F}}_a + \left(\mathbb{I} - \frac{\Delta t}{2}\tilde{\mathcal{C}}_a\right)^{-1}\left(\mathbb{I} + \frac{\Delta t}{2}\tilde{\mathcal{C}}_a\right)\right]\tilde{\Psi}_a(x,t),$$

where $\mathbb{I}$ is the identity matrix and $\tilde{\Psi}_a^*(x,t)$ denotes an auxiliary field,

$$\tilde{\mathcal{C}}_a = \frac{1}{2}X_a^\dagger \mathcal{C} X_a = -\frac{i}{D}m(X_a^\dagger\gamma^0 X_a) - \gamma^0 e_a^i \Gamma_i, \tag{A8}$$

$$\tilde{\mathcal{F}}_a\tilde{\Psi}_a(x,t) = \left(e_a^i - \delta_a^i\right)[\tilde{\Psi}_a(x \mp n_i\Delta t, t) - \tilde{\Psi}_a(x,t)], \tag{A9}$$

where n_i is the lattice direction and $\mathcal{C}$ is the collision term, Eq. (A4). The upper sign applies to the spin-up components (Ψ_1^+, Ψ_2^+), and the lower sign applies to the spin-down components (Ψ_1^-, Ψ_2^-).

(3) **Streaming:** The spinor components are streamed to the closest grid points along the lattice direction $\pm n_a$,

$$\tilde{\Psi}_a\left(x, t+\frac{\Delta t}{2}\right) = \tilde{\Psi}_a^*(x \mp n_a\Delta t, t). \tag{A10}$$

(4) **Inverse rotation:** The spinor is rotated back via X_a,

$$\Psi_a\left(x, t+\frac{\Delta t}{2}\right) = X_a\tilde{\Psi}_a\left(x, t+\frac{\Delta t}{2}\right). \tag{A11}$$

(5) Repeat steps 2–4 for the next spatial direction.

The external potentials $V(x)$, a scalar, and $A(x)$, a vector, are added to the collision operator (A8), such that

$$\tilde{\mathcal{C}}_a = \frac{1}{2}X_a^\dagger \mathcal{C} X_a = -\frac{i}{D}(m-V)(X_a^\dagger\gamma^0 X_a) - \gamma^0 e_a^i(\Gamma_i - iA_i). \tag{A12}$$

The simulation for strained graphene is carried out with modified Eqs. (A8) and (A9), according to the following scheme:

$$\tilde{\mathcal{C}}_a \to \sqrt{g}\tilde{\mathcal{C}}_a,\ e_a^i \to \sqrt{g}e_a^i.$$

The additional factor $\sqrt{g}$ originates from the volume element of the Hamiltonian (2).

APPENDIX B: RIEMANNIAN GEOMETRY

The Latin indices run over the spatial dimensions, and Einstein summation convection is used for repeated indices.

A D-dimensional curved space is represented by a Riemannian manifold M, which is locally described by a smooth diffeomorphism $\mathbf{h}$, called the chart. The set of tangential vectors attached to each point $\mathbf{y}$ on the manifold is called the tangent space $T_\mathbf{y}M$. In the fluid model, all the vector quantities are represented as elements of $T_\mathbf{y}M$. The derivatives of the chart $\mathbf{h}$ are used to define the standard basis $(\mathbf{e}_1, \ldots, \mathbf{e}_D) = \frac{\partial\mathbf{h}}{\partial x^1}, \ldots, \frac{\partial\mathbf{h}}{\partial x^D}$.

The metric tensor g can be used to measure the length of a vector or the angle between two vectors. In local coordinates, the components of the metric tensor are given by

$$g_{ij}(x) = \mathbf{e}_i(x)\cdot\mathbf{e}_j(x) = \frac{\partial\mathbf{h}}{\partial x^i}\cdot\frac{\partial\mathbf{h}}{\partial x^j}, \tag{B1}$$

where the center dot $(\cdot)$ is the standard Euclidean scalar product.

For a given metric tensor, the vector $v = v^i\mathbf{e}_i \in T_\mathbf{y}M$ has a norm $||v||_g = \sqrt{v^i g_{ij} v^j}$ and a corresponding dual vector $v^* = v^i\mathbf{e}_i \in T_\mathbf{y}^*M$ in the cotangent space, which is spanned by the differential 1-forms $dx^i = g(\mathbf{e}_i, \cdot)$. The coefficients v_i of the dual vector are typically denoted by a lower index and are related to the upper-index coefficients v^i by contraction with the metric tensor $v_i = g_{ij}v^j$, or, equivalently, $v^i = g^{ij}v_j$, where g^{ij} denotes the inverse of the metric tensor. The upper-index coefficients v^i of a vector v are typically called *contravariant components*, whereas the lower-index coefficients v_i of the dual vectors v^* are known as the *covariant components*.

A necessary feature for the description of objects moving on the manifold is parallel transport of vectors along the manifold. The tangent space is equipped with a covariant derivative $\boldsymbol{\nabla}$ (Levi-Civita connection), which connects the tangent spaces at different points on the manifold and thus allows us to transport a tangent vector from one tangent space to the other along a given curve $\gamma(t)$. The covariant derivative can be viewed as the orthogonal projection of the Euclidean derivative ∂ onto the tangent space, such that the tangency of the vectors is preserved during the transport. In local coordinates, the covariant derivative is fully characterized by its connection coefficients Γ_{jk}^i (Christoffel symbols), which are defined by the action of the covariant derivative on the basis vector, $\boldsymbol{\nabla}_j\mathbf{e}_k = \Gamma_{jk}^i$. In the standard basis, $\mathbf{e}_i = \frac{\partial\mathbf{h}}{\partial x^i}$, the Christoffel symbols are related to the metric by

$$\Gamma_{jk}^i = \tfrac{1}{2}g^{ij}(\partial_j g_{kl} + \partial_k g_{jl} - \partial_l g_{jk}). \tag{B2}$$

Acting on a general vector $v = v^i\mathbf{e}_i$, the covariant derivative becomes

$$\boldsymbol{\nabla}_k v = \left(\partial_k v^i + \Gamma_{kj}^i v^j\right)\mathbf{e}_i, \tag{B3}$$

where the product rule has been applied, using the fact that the covariant derivative acts as a normal derivative on the scalar functions v^i. Extending to tensors of higher rank, for example, the second-order tensors $T = T^{ij}$,

$$\boldsymbol{\nabla}_k T = \left(\partial_k T^{ij} + \Gamma_{kl}^i T^{lj} + \Gamma_{kl}^j T^{il}\right)\mathbf{e}_i \otimes \mathbf{e}_j, \tag{B4}$$

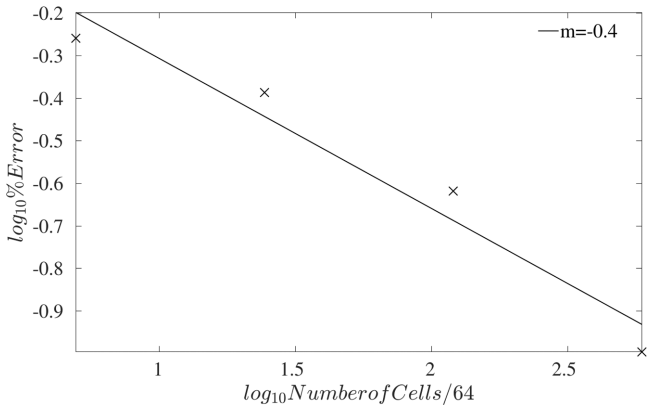

FIG. 5. Error convergence of the proposed quantum lattice Boltzmann closed boundary condition. The logarithm of the relative error of the density ρ is plotted against the normalized logarithmic number of cells. m denotes the gradient.

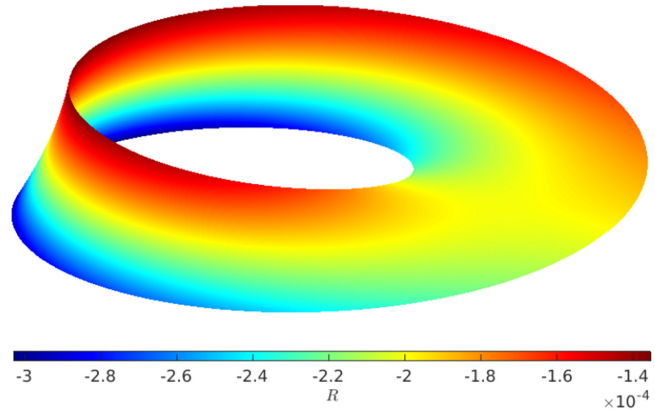

FIG. 6. The Ricci scalar of the Möbius strip for half-width $w = 0.1$ and a midcircle of radius $R = 1$.

in this work the basis vectors $\mathbf{e}_i$ are generally dropped. The compatibility of the covariant derivative with the metric tensor implies that $\nabla_k g^{ij} = \nabla_k g_{ij} = 0$. This property allows us to commute the covariant derivative with the metric tensor for the raising or lowering of tensor indices in derivative expressions.

The motion of the particle can be described by the curve $\gamma(t)$, which parametrizes the position of the particle at time t. The geodesic equation, $\nabla_{\dot\gamma}\dot\gamma = 0$, in local coordinates $\gamma(t) = \gamma^i(t)\mathbf{e}_i$ is defined by

$$\ddot\gamma^i + \Gamma^i_{jk}\dot\gamma^j\dot\gamma^k = 0. \tag{B5}$$

The geodesic equation can be interpreted as the generalization of Newton's law of inertia to curved space. The solutions of Eq. (B5) represent lines of constant kinetic energy on the manifold, i.e., the geodesics. The Riemann curvature tensor R can be used to measure curvature, or more precisely, it measures curvature-induced change in a tangent vector v when transported along a closed loop,

$$R(\mathbf{e}_i, \mathbf{e}_j)v = \nabla_i\nabla_j v - \nabla_j\nabla_i v. \tag{B6}$$

In a local coordinate basis $\mathbf{e}_i$, the coefficients of the Riemann curvature tensor are given by

$$R^l_{ijk} = g(R(\mathbf{e}_i, \mathbf{e}_j)\mathbf{e}_k, \mathbf{e}_l) \tag{B7}$$

$$= \partial_j\Gamma^l_{ik} - \partial_k\Gamma^l_{ij} + \Gamma^l_{jm}\Gamma^m_{ik} - \Gamma^l_{km}\Gamma^m_{ij}. \tag{B8}$$

Contraction of R^i_{jkl} to rank 2 and 1 tensors yields the Ricci tensor $R_{ij} = R^k_{ikj}$ and the Ricci scalar $R = g^{ij}R_{ij}$, respectively, which can also be used to quantify curvature.

The gradient is defined as $\nabla^i f = g^{ij}\partial_j f$, the divergence is defined as $\nabla_i v^i = \frac{1}{\sqrt{g}}\partial_i(\sqrt{g}v^i)$, and the integration over curved volume is defined as $V = \int_V Q dV$, where $dV = \sqrt{g}dx^1\cdots dx^D =: \sqrt{g}d^Dx$ denotes the volume element. $\sqrt{g}$ denotes the square root of the determinant of the metric tensor.

It should be clarified that in the simulations there is no time curvature and g_{ij} denotes the curved-space metric.

APPENDIX C: CONVERGENCE OF THE CLOSED DIRAC BOUNDARY CONDITIONS

The convergence of the proposed quantum lattice Boltzmann boundary condition is shown in Fig. 5.

APPENDIX D: RICCI SCALAR FOR THE MÖBIUS STRIP

The Ricci scalar for the Möbius strip is nonzero across the whole domain for the specific choice of parameters as shown in Fig. 6.

[1] F. D. M. Haldane, Nobel lecture: Topological quantum matter, Rev. Mod. Phys. **89**, 040502 (2017).

[2] X.-L. Qi and S.-C. Zhang, Topological insulators and superconductors, Rev. Mod. Phys. **83**, 1057 (2011).

[3] J. Wang and S.-C. Zhang, Topological states of condensed matter, Nat. Mater. **16**, 1062 (2017).

[4] R. Takahashi, *Topological Invariant and Topological Phases* (Springer, Tokyo, Japan, 2015), p. 5.

[5] S. Stützer, Y. Plotnik, Y. Lumer, P. Titum, N. H. Lindner, M. Segev, M. C. Rechtsman, and A. Szameit, Photonic topological anderson insulators, Nature (London) **560**, 461 (2018).

[6] A. K. Geim and K. S. Novoselov, The rise of graphene, Nat. Mater. **6**, 183 (2007).

[7] A. K. Geim, Graphene: Status and prospects, Science **324**, 1530 (2009).

[8] S. Das Sarma, S. Adam, E. H. Hwang, and E. Rossi, Electronic transport in two-dimensional graphene, Rev. Mod. Phys. **83**, 407 (2011).

[9] Z. Jiang, Y. Zhang, Y.-W. Tan, H. Stormer, and P. Kim, Quantum Hall effect in graphene, Solid State Commun. **143**, 14 (2007).

[10] C. L. Kane and E. J. Mele, Quantum Spin Hall Effect in Graphene, Phys. Rev. Lett. **95**, 226801 (2005).

[11] F. D. M. Haldane, Model for a Quantum Hall Effect without Landau Levels: Condensed-Matter Realization of the "Parity Anomaly," Phys. Rev. Lett. **61**, 2015 (1988).
[12] M. Büttiker, Edge-state physics without magnetic fields, Science **325**, 278 (2009).
[13] J. Simon, Magnetic fields without magnetic fields, Nature (London) **515**, 202 (2014).
[14] E. W. S. Caetano, V. N. Freire, S. G. dos Santos, D. S. Galvao, and F. Sato, Möbius and twisted graphene nanoribbons: Stability, geometry, and electronic properties, J. Chem. Phys. **128**, 164719 (2008).
[15] Z. Geng, B. Xiong, L. Wang, K. Wang, M. Ren, L. Zhang, J. Zhu, and Z. Yang, Möbius strips of chiral block copolymers, Nat. Commun. **10**, 4090 (2019).
[16] Z. L. Guo, Z. R. Gong, H. Dong, and C. P. Sun, Möbius graphene strip as a topological insulator, Phys. Rev. B **80**, 195310 (2009).
[17] Y. Liu, L.-R. Ding, A.-L. He, and Y.-F. Wang, Quantum transport in Chern insulators on Möbius strips, J. Phys.: Condens. Matter **32**, 505501 (2020).
[18] W. Beugeling, A. Quelle, and C. Morais Smith, Nontrivial topological states on a Möbius band, Phys. Rev. B **89**, 235112 (2014).
[19] G. Di Molfetta, M. Brachet, and F. Debbasch, Quantum walks as massless Dirac fermions in curved space-time, Phys. Rev. A **88**, 042301 (2013).
[20] A. Cortijo and M. A. H. Vozmediano, Electronic properties of curved graphene sheets, Europhys. Lett. **77**, 47002 (2007).
[21] Z. Li and L. R. Ram-Mohan, Quantum mechanics on a Möbius ring: Energy levels, symmetry, optical transitions, and level splitting in a magnetic field, Phys. Rev. B **85**, 195438 (2012).
[22] N. Zhao, H. Dong, S. Yang, and C. P. Sun, Observable topological effects in molecular devices with Möbius topology, Phys. Rev. B **79**, 125440 (2009).
[23] F. Guinea, M. I. Katsnelson, and A. K. Geim, Energy gaps and a zero-field quantum Hall effect in graphene by strain engineering, Nat. Phys. **6**, 30 (2010).
[24] J.-D. Debus, Flows in curved spaces, Ph.D. thesis, ETH Zürich, 2016.
[25] K. Flouris, M. Mendoza Jimenez, J.-D. Debus, and H. J. Herrmann, Confining massless Dirac particles in two-dimensional curved space, Phys. Rev. B **98**, 155419 (2018).
[26] S. Succi and R. Benzi, Lattice Boltzmann equation for quantum mechanics, Phys. D (Amsterdam, Neth.) **69**, 327 (1993).
[27] A. H. Castro Neto, F. Guinea, N. M. R. Peres, K. S. Novoselov, and A. K. Geim, The electronic properties of graphene, Rev. Mod. Phys. **81**, 109 (2009).
[28] M. Oliva-Leyva and G. G. Naumis, Generalizing the Fermi velocity of strained graphene from uniform to nonuniform strain, Phys. Lett. A **379**, 2645 (2015).
[29] J.-D. Debus, M. Mendoza, and H. J. Herrmann, Shifted Landau levels in curved graphene sheets, J. Phys.: Condens. Matter **30**, 415503 (2018).
[30] A. R. Akhmerov and C. W. J. Beenakker, Boundary conditions for Dirac fermions on a terminated honeycomb lattice, Phys. Rev. B **77**, 085423 (2008).
[31] D. Xiao, M.-C. Chang, and Q. Niu, Berry phase effects on electronic properties, Rev. Mod. Phys. **82**, 1959 (2010).
[32] K. Flouris, S. Succi, and H. J. Herrmann, Quantized alternate current on curved graphene, Condens. Matter **4**, 39 (2019).
[33] Y. Aharonov and D. Bohm, Significance of electromagnetic potentials in the quantum theory, Phys. Rev. **115**, 485 (1959).
[34] S. Tanda, T. Tsuneta, Y. Okajima, K. Inagaki, K. Yamaya, and N. Hatakenaka, A Möbius strip of single crystals, Nature (London) **417**, 397 (2002).
[35] G. Ouyang, L. Ji, Y. Jiang, F. Würthner, and M. Liu, Self-assembled Möbius strips with controlled helicity, Nat. Commun. **11**, 5910 (2020).
[36] A. Johansson, P. Myllyperkiö, P. Koskinen, J. Aumanen, J. Koivistoinen, H.-C. Tsai, C.-H. Chen, L.-Y. Chang, V.-M. Hiltunen, J. J. Manninen, W. Y. Woon, and M. Pettersson, Optical forging of graphene into three-dimensional shapes, Nano Lett. **17**, 6469 (2017).
[37] P. Han, K. Akagi, F. Federici Canova, R. Shimizu, H. Oguchi, S. Shiraki, P. S. Weiss, N. Asao, and T. Hitosugi, Self-assembly strategy for fabricating connected graphene nanoribbons, ACS Nano **9**, 12035 (2015).